2012

Validation of Shear-Wave Velocity Models of the Pacific Northwest

Haiying Gao
University of Rhode Island

Yang Shen
University of Rhode Island, yshen@uri.edu

Citation/Publisher Attribution
Haiying Gao, Yang Shen; Validation of Shear-Wave Velocity Models of the Pacific Northwest. *Bulletin of the Seismological Society of America* ; 102 (6): 2611–2621. doi: https://doi.org/10.1785/0120110336
Available at: https://doi.org/10.1785/0120110336

Bulletin of the Seismological Society of America, Vol. 102, No. 6, pp. 2611–2621, December 2012, doi: 10.1785/0120110336

Validation of Shear-Wave Velocity Models of the Pacific Northwest

by Haiying Gao and Yang Shen

Abstract Four surface-wave tomographic models in the Pacific Northwest and a combined CRUST2.0 and AK135 model are tested and validated systematically. Synthetic Green's functions calculated with the models using a finite-difference method are compared with empirical Green's functions at periods of 7–50 s. To ensure high-quality signals, empirical Green's functions are extracted from the ambient noise cross correlation of vertical-to-vertical components between station pairs that have up to a decade of recorded data. The observed and synthetic Green's functions are cross correlated at multiple frequency bands to determine phase delay times and cross-correlation coefficients. The delay time predicted by the CRUST2.0 and AK135 model is predominantly positive and is linearly dependent on interstation distance, indicating that the combined model is, on average, too fast for the Pacific Northwest. Among the four shear-wave velocity models, CUB and one model derived from regional tomography exhibit moderately and weakly negative linear trends, respectively, between the delay time and interstation distance, a result indicative of a slower-than-actual velocity. The delay times of the other two models are normally distributed with an approximately zero mean and without any apparent relationship with interstation distance. The cross-correlation coefficients are more scattered at short periods, reflecting unresolved heterogeneities of the crust structure in these models. The misfit between the empirical Green's functions and synthetic waveforms suggests the need for a better-resolved crust and uppermost mantle velocity model, which is critical for the precise estimate of ground motion for seismic hazard evaluation and understanding of the tectonic processes of the Pacific Northwest.

Introduction

In recent years, the crust and upper mantle of the western United States have been imaged in numerous studies (e.g., Burdick *et al.*, 2008; Roth *et al.*, 2008; Yang *et al.*, 2008; Moschetti *et al.*, 2010; Schmandt and Humphreys, 2010; Wagner *et al.*, 2010; Calkins *et al.*, 2011; Calvert *et al.*, 2011; Gao *et al.*, 2011; Porritt *et al.*, 2011). The resulting models vary in station coverage and resolution. Yang *et al.* (2008) constructed an isotropic shear-wave velocity model from an integration of ambient noise and earthquake surface-wave tomography. The lateral resolution of their model is estimated to be ~70 km on average, comparable to the spacing of the EarthScope Transportable Array stations used in their study. Moschetti *et al.* (2010) updated this model by considering both Rayleigh and Love waves and radial anisotropy. By including the EarthScope Transportable Array and a few regional EarthScope flexible arrays, Gao *et al.* (2011), Calkins *et al.* (2011), and Porritt *et al.* (2011) constructed crustal models from ambient noise tomography that have a denser ray-path coverage than the Yang *et al.* (2008) and Moschetti *et al.* (2010) models. The Cascadian model by Porritt *et al.* (2011) has an estimated spatial resolution of 150 km along geographic longitude and latitude to 120 km depth. Calkins *et al.* (2011) focused on the northern Cascadia crust and obtained an estimated horizontal resolution of ~50 km. In general, the imaged crust and uppermost mantle structure in these models correlates well with regional-scale tectonics and helps in our understanding of the tectonic evolution in the Pacific Northwest.

There are also major limitations in the recent shear-wave velocity models. First, as is commonly performed, surface-wave dispersion curves are retrieved from the ambient noise cross correlation between two stations (e.g., Yao *et al.*, 2006; Bensen *et al.*, 2007; Ekström *et al.*, 2009) and then inverted to obtain the phase and/or group velocities at each map location (e.g., Montagner, 1986; Barmin *et al.*, 2001; Villaseæor *et al.*, 2007; Stankiewicz *et al.*, 2010). To construct a shear-wave velocity model, the phase/group velocity at each map node is inverted to obtain a 1D velocity profile. This two-step inversion procedure does not fully account for the 3D nature of wave propagation and interaction and may lead to unrealistic and/or inconsistent local artifacts. Second, there exists a velocity–depth trade-off between the selected depth of velocity discontinuities and wavespeed near the interface (e.g., Yang *et al.*, 2008; Yao *et al.*, 2008; Gao *et al.*, 2011; Porritt

et al., 2011). Third, inversions are carried out under the assumption that Rayleigh waves are not affected by *P*-wave speed, which is inaccurate especially at shallow depth (Simons and van der Hilst, 2003; Lebedev and van der Hilst, 2008; Zhang and Shen, 2008). Therefore, the accuracy of these velocity models is uncertain. Quantifying the accuracy of the velocity models helps quantify uncertainties in geodynamic interpretations and improves the prediction of strong ground motion for seismic-hazard evaluation (Ma *et al.*, 2008; Bozdag and Trampert, 2010; Maceira *et al.*, 2010). Thus, testing and validation of the existing shear-wave velocity models for the Pacific Northwest are needed.

In this study, we simulate wave propagation with a 3D finite-difference method (Zhang *et al.*, 2011) and directly compare empirical Green's functions (EGFs) and synthetics. We select five models: CRUST2.0 (Bassin *et al.*, 2000), CUB (a $2° \times 2°$ upper-mantle shear-wave velocity model by Shapiro and Ritzwoller [2002]), and three regional shear-wave velocity models by Yang *et al.* (2008), Gao *et al.* (2011), and Porritt *et al.* (2011). Hereinafter, we refer to these models

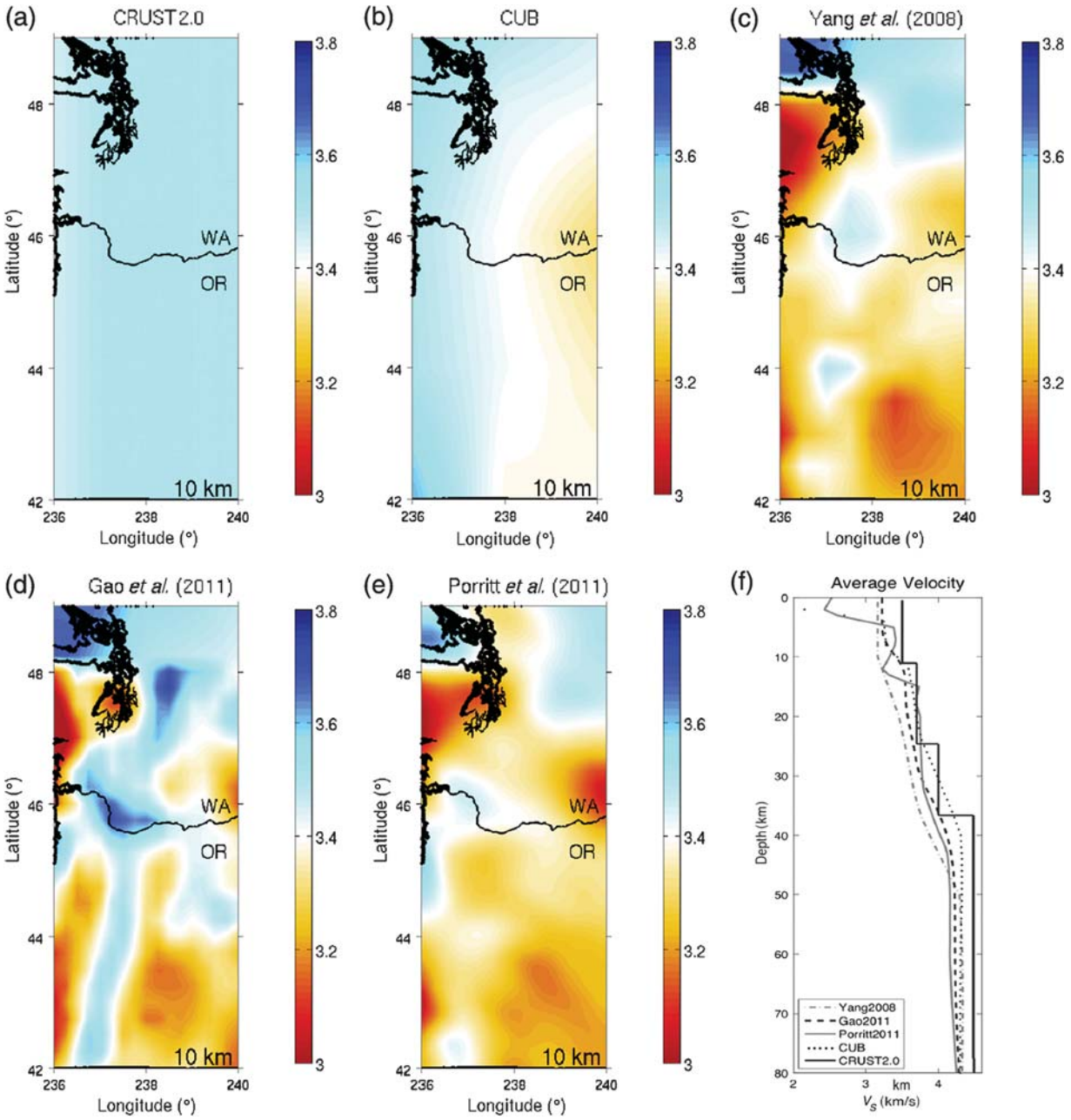

Figure 1. (a)–(e) Horizontal slices of the five shear-wave velocity models tested in this study at 10 km depth. All of these five panels share the same color scale in km/s. (f) The average 1D shear-wave velocity profiles for the five models. CRUST2.0 is shown as a layered velocity, and the velocity of the other models are depth interpolated.

as CRUST2.0, CUB, Yang2008, Gao2011, and Porritt2011, respectively. All of the three regional models are extended to 200 km depth and merged with AK135 at depths greater than the original depths of the corresponding models. Shear-wave velocity is converted to *P*-wave velocity with a V_P/V_S ratio of 1.74 in the crust (Brocher, 2005) and the empirical relationship of V_P and V_S in the mantle with corresponding depths (Kennett *et al.*, 1995). The density is calculated as a function of V_P (Christensen and Mooney, 1995). See Figure 1 for horizontal slices of these five models in the crust and their 1D average velocity profiles.

In the following, we first briefly introduce the EGFs used in this study. Then, we discuss wave propagation simulation and compare observed and synthetic waveforms. We find a linear dependence of delay time on interstation distance for CRUST2.0 (positive), CUB (moderately negative), and Porritt2011 (weakly negative), which indicates that these three models are on average faster, slower, and slower, respectively, than the real Earth in the Pacific Northwest. Yang2008 and Gao2011 predict more accurate phase arrivals without displaying any obvious relationship between delay time and interstation distance.

Extraction of Empirical Green's Functions

To retrieve the EGFs between station pairs, we use continuous seismic data recorded between 1995 and 2011 by about 220 stations in an area extending from northernmost California to central Washington (Fig. 2). All of the data are requested from the Incorporated Research Institutions

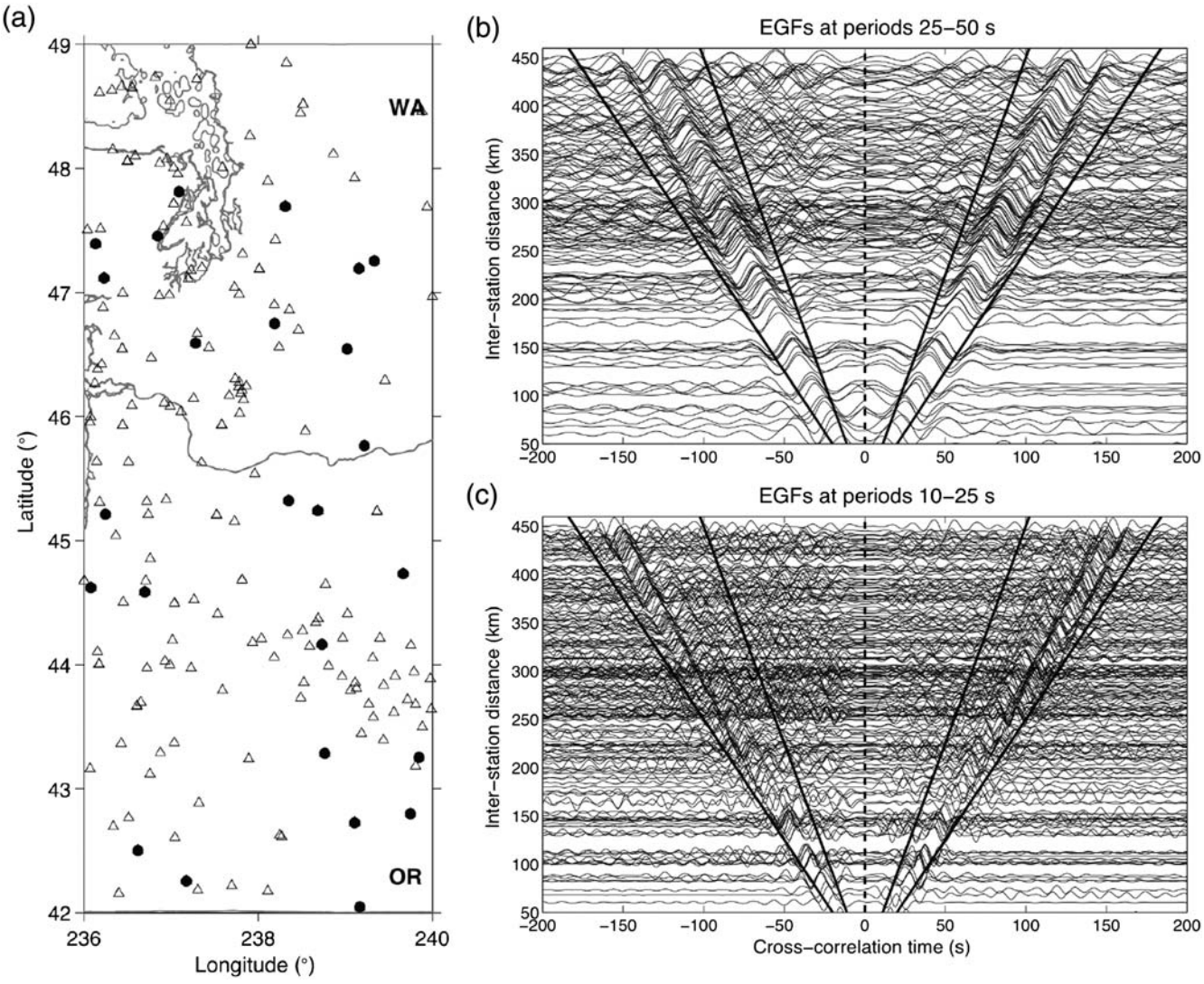

Figure 2. (a) Distribution of the stations used in this study, which include the EarthScope Transportable Array (TA), the Pacific Northwest regional seismic network (UW), the United States national seismic network (US), the Plate Boundary Observatory Borehole seismic network (PB), and a few flexible arrays. The dots represent the virtual sources used in wave simulation, and the triangles show the receivers. (b)–(c) EGFs derived from ambient noise cross correlation of vertical-to-vertical components are plotted by the interstation distance, filtered at 25–50 and 10–25 s, respectively. The solid lines mark approximately the time window for waves with the group velocity in the 2.5–4.5 km/s range.

for Seismology (IRIS) Data Management Center. Prior to cross correlation of ambient noise, we remove instrument response, cut the continuous record into a daily length, and resample the waveform to a uniform sample rate of 1 point per second. To normalize ambient noise in the time and frequency domains, we filter the records at frequency bands of 1 mHz width, normalize the resulting signals with their envelopes, and then sum the normalized signals into frequency–time-normalized (FTN) waveform (Ekström *et al.*, 2009). Unlike the commonly used one-bit and running-absolute-mean normalizations (Bensen *et al.*, 2007), the FTN waveform adjusts to temporal variations in signal spectrum and yields a flat spectrum at all times (Shen *et al.*, 2012). To further reduce the effect of earthquakes, segments of data with large earthquakes ($M > 5.0$) are tapered off. For each station pair, daily cross correlation of vertical-to-vertical components is stacked in order to increase the signal-to-noise ratio. The EGFs are recovered as the time derivative of the stacked cross correlations (e.g., Snieder, 2004; Sabra *et al.*, 2005) and have good signal-to-noise ratio at periods of 7–200 s (Fig. 2). For the periods of interest, the EGFs from the cross correlation of vertical–vertical channels are primarily Rayleigh waves. Considering the depth resolution of the five models to be tested, we focus on periods of 7–50 s in this study.

Finite-Difference Wave Simulation

We implement a 3D nonstaggered-grid, finite-difference method to simulate wave propagation in the 3D spherical Earth structure (Zhang *et al.*, 2011). No anisotropy and attenuation are considered in the simulation. The horizontal grid spacing is ~1.6 km along geographic longitude and latitude. The vertical grid spacing is depth dependent with finer grids in the crust, ~0.5 km near the surface, and increasing to 2 km at 100 km depth. Such a grid is sufficient to accurately simulate wave propagation at 7 s and longer periods (see Zhang *et al.*, 2011). To maintain numerical stability, we use a time step of 0.1 s and run a total of 5000 time steps (that is, 500 s wave propagation time). The source function is a Gaussian pulse with a half width of 3 s. To test and validate the accuracy of the models in a systematic way, we choose 25 widely distributed seismic stations as virtual sources (dots in Fig. 2) and all of the others as receivers (~200 stations, triangles in Fig. 2). The 3D wave simulation is executed on a Linux cluster with 26 nodes (each with four CPU cores). It takes about nine hours per simulation at one node. The predicted ground motion on the surface in response to the virtual sources differs for these five models. The synthetic Green's functions, from each virtual source station to other stations, are extracted.

Prior to comparing the EGFs and synthetics, we first split the EGFs into positive (causal) and negative (acausal) time lags, and convolve the EGFs with the source–time function used in wave simulation. The convolution accounts for the effect of the source–time function in the simulation. The EGFs and synthetic waveforms are filtered at multiple frequency bands ranging from 25–50 s, 15–35 s, 10–25 s, and 7–15 s. The signal-to-noise ratio of the EGFs must be at least 7 to satisfy a high-quality signal criterion. Here, the signal is referred to as the maximum amplitude within the selected signal window (defined by approximate wave group velocities), and the noise is defined as the maximum standard error of the mean of the monthly EGFs within the same time window (see Fig. 3). We then cross correlate the positive- and negative-time-lag EGFs with the corresponding synthetics at the four frequency bands (see an example in Fig. 4). The maximum cross-correlation lag time is limited to be within ±10% perturbation of the reference arrival time (calculated as the interstation distance divided by the group velocity of 3.9 km/s). The phase delay time is the average of the measurements for the positive and negative time lags, which minimizes the effect of the instrument time shift, if it exists (Stehly *et al.*, 2007). Figure 5 displays the comparison of the EGFs and synthetics from one virtual source to other receivers.

To quantify the accuracy of the models, we consider the chi-squared value χ^2, which is defined as

$$\sum_{i=1}^{N}\left(\frac{\mathrm{d}t_i}{\sigma_i}\right)^2 = \chi^2, \tag{1}$$

where σ_i is the uncertainty of phase delay time $\mathrm{d}t_i$ between the EGFs and synthetics at the ith station pair, and N is the total number of measurements. Here, the data uncertainty σ_i accounts for the temporal variation of the signal, which is defined as the standard error of the mean delay time between

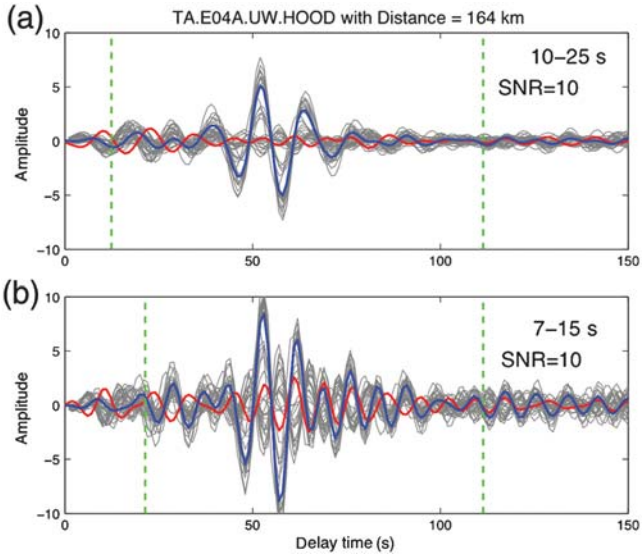

Figure 3. Definition of the frequency-dependent signal-to-noise ratio at periods of (a) 10–25 s and (b) at 7–15 s. The EGFs at positive and negative lag times, retrieved from stacked cross correlations, are displayed as thick blue and red lines, respectively. Each gray trace represents an EGF extracted from monthly-stacked cross correlations (a total of 17 months). The signal-to-noise ratio is defined as the maximum amplitude within the signal window (the vertical dashed lines) divided by the maximum standard error of the mean of the monthly EGFs, and the average of the values for the positive and negative time lags.

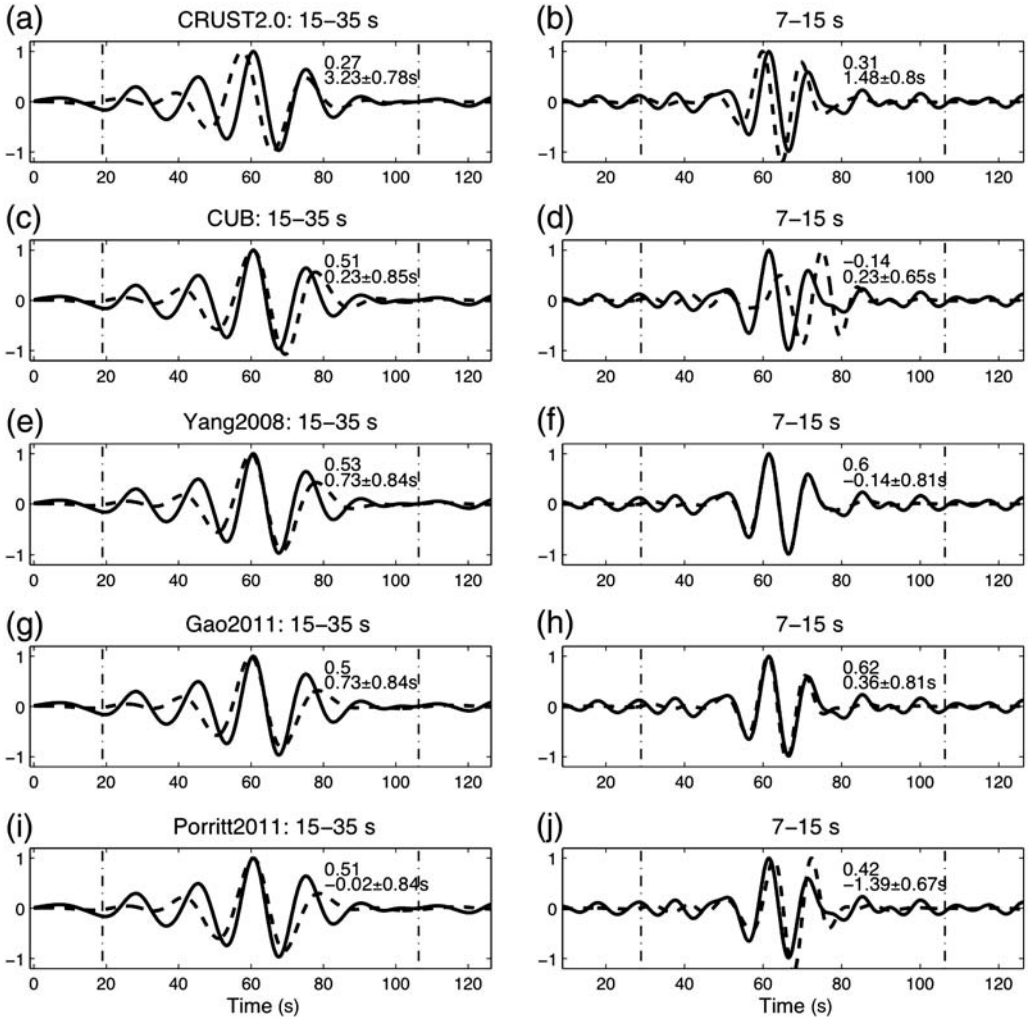

Figure 4. Example of synthetic waveforms (dashed lines) and EGFs (solid lines). Five velocity models (each row) are tested in the wave simulation at multiple frequency bands (each column): (a)–(b) CRUST2.0, (c)–(d) CUB, and three regional shear-wave velocity models by (e)–(f) Yang *et al.* (2008), (g)–(h) Gao *et al.* (2011), and (i)–(j) Porritt *et al.* (2011). The cross-correlation coefficient and phase delay time with uncertainty are denoted inside each panel.

the monthly EGFs and synthetics. We normalize the χ^2 value by the number of measurements N. Typically, $\chi^2/N = 1$ indicates a model that adequately predicts the data (see the discussion in Montelli *et al.*, 2004).

Cross-Correlation Results of EGFs and Synthetics

Under the criteria of a signal-to-noise ratio greater than 7 and at least a 1.5-wavelength station separation, the number of measurements varies from a few hundred to more than a thousand from long to short periods. In the following, we compare the five models in three ways: phase delay time versus interstation distance (Fig. 6), histograms of phase delay times (Fig. 7), and histograms of cross-correlation coefficients (Fig. 8). The synthetic waveforms from an accurate model should fit the EGFs well, resulting in nearly zero phase delay time and a high cross-correlation coefficient. Here, a positive delay time means that the arrival in the synthetics is earlier than in the EGFs. Positive cross-correlation coefficients indicate that the phase lag time is less than one-fourth of the central period. In general, the delay time increases linearly with interstation distance for CRUST2.0 and decreases slightly for CUB and Porritt2011, while there is no obvious trend for Yang2008 and Gao2011.

CRUST2.0

As shown in Figure 6, the phase delay time predicted by CRUST2.0 is linearly dependent on the interstation distance and is dominantly positive at all the frequency bands (the first row of Figs. 6 and 7). To verify that this linear trend is not an artifact caused by the absolute lag time criterion (less than 10% of the reference arrival time, as bounded by the solid lines in Fig. 6), we check the distribution pattern by including all measurements with signal-to-noise ratios greater than 7 (open circles in Fig. 6). Without the absolute lag time criterion, the data become more scattered, particularly at short periods. Some of the measurements with

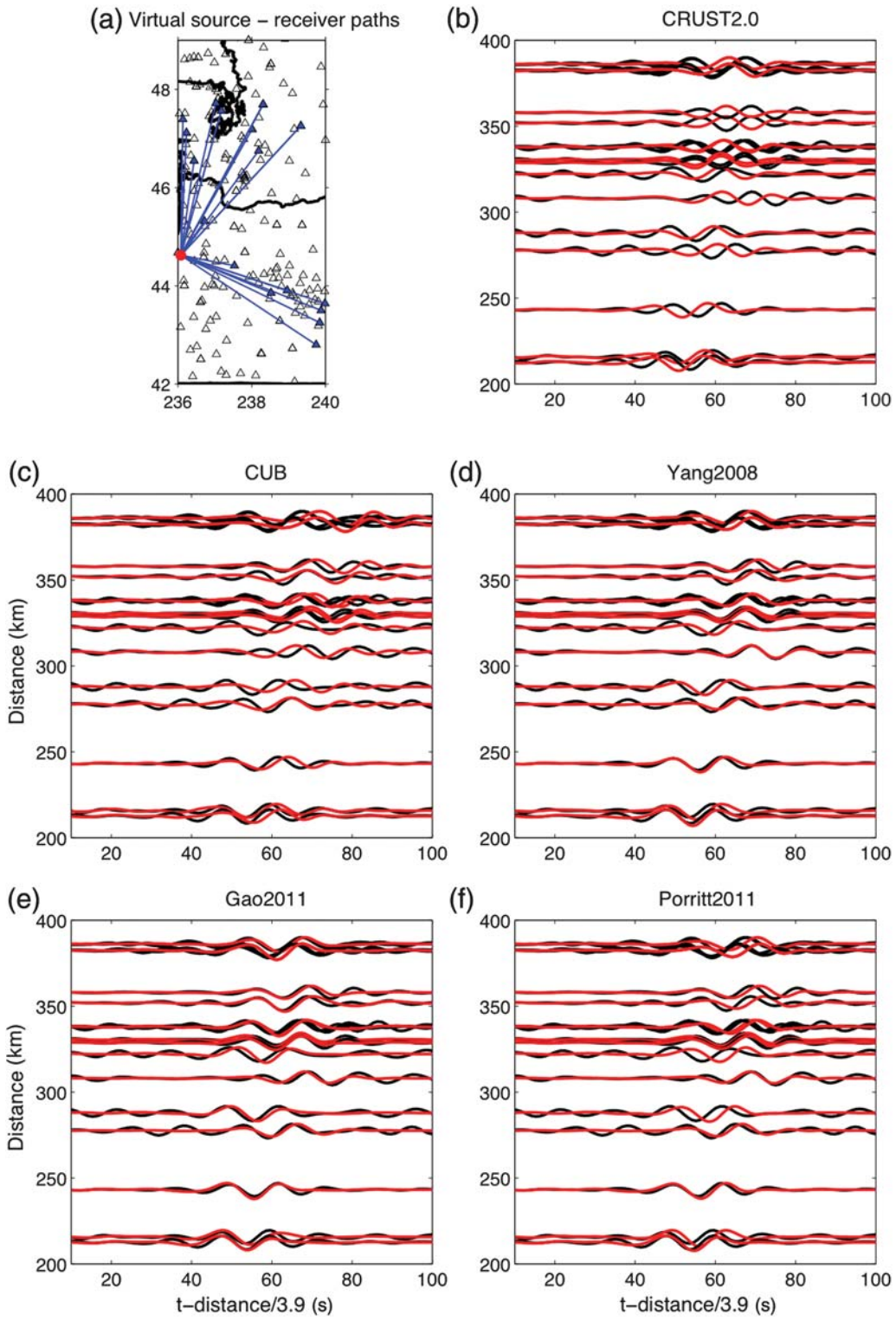

Figure 5. (a) The lines connect the receiver stations (blue triangles) to the source station (red dot). The blank triangles show all of the stations in this study as in Figure 2. (b)–(f) A comparison of synthetic waveforms (red lines) with EGFs (black lines) for the five models. The waveforms are filtered at 10–25 s. The x axis is time shifted with the interstation distance divided by the reference group velocity, 3.9 km/s.

large absolute delays may be caused by phase skipping. Nevertheless, the majority of the measurements show a linear dependence of delay time on interstation distance. In the following, our discussion focuses on measurements with absolute lag times less than 10% of the reference arrival time for all models. The dominance of positive phase delay times implies that the average velocity of the combined model of CRUST2.0 in the crust and AK135 in the upper mantle is too

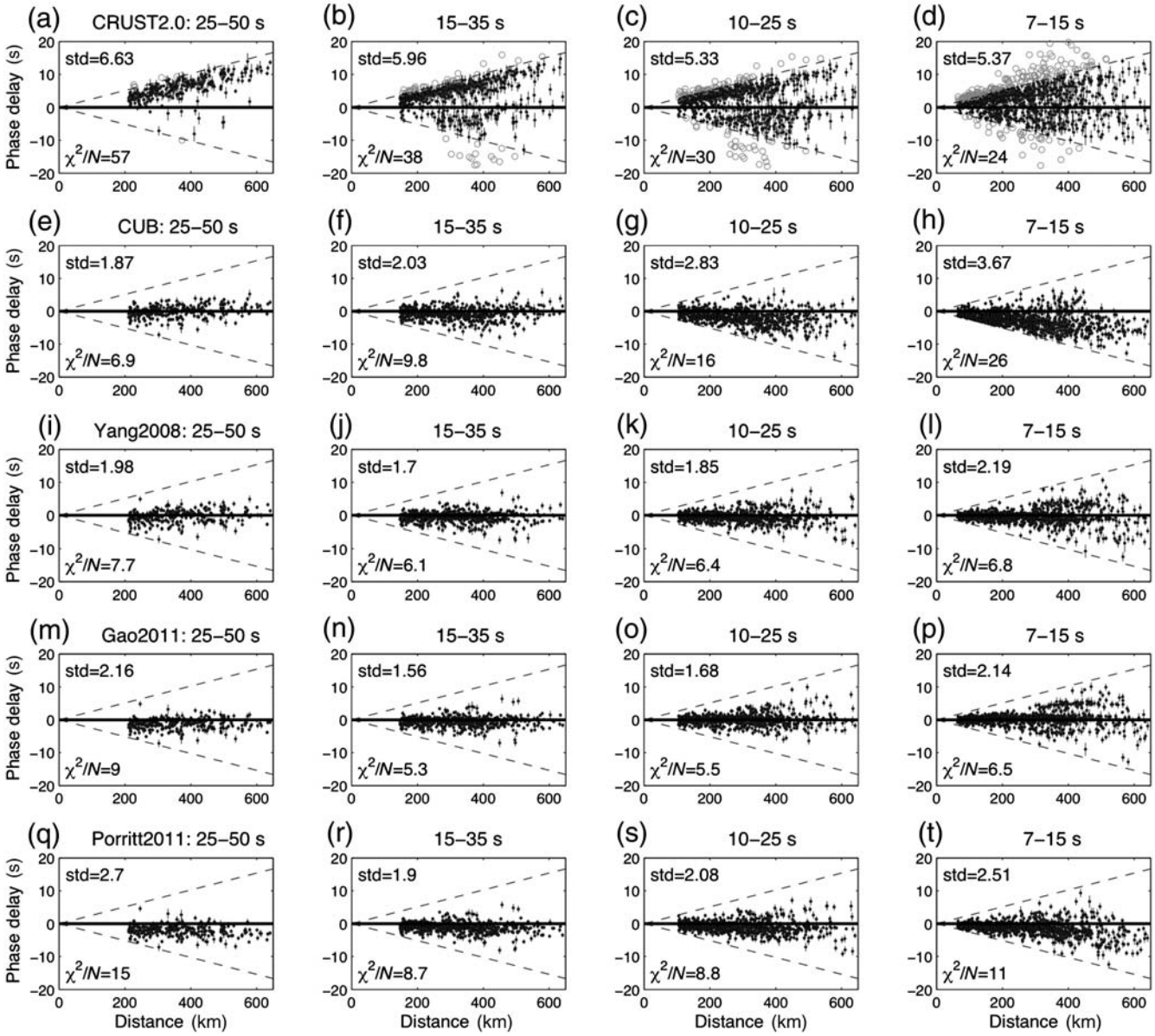

Figure 6. Travel-time delay versus interstation distance at four frequency bands (each column) for five models (each row). The standard deviation of the travel-time delay with respect to zero mean (solid lines) and the normalized chi-squared value are denoted in each panel. The dashed lines limit the maximum perturbation of lag time, which is 10% of the reference arrival time (calculated as the distance divided by the group velocity of 3.9 km/s). The gray circles in the first row are measurements with absolute lag times larger than 10% of the reference arrival time for CRUST2.0.

fast for the Pacific Northwest. Consequently, the phase is progressively delayed with distance. At short periods, a portion of the delay times is negative. The sensitivity depth of Rayleigh waves at these periods corresponds to the upper and middle crust; thus, the negative lag time may indicate local shallow velocities in the model that are too low.

The normalized χ^2/N value, calculated with equation (1), ranges from 19 and 30 (Fig. 6), which indicates a poor velocity model for the study area. Also, as indicated by the histograms of the cross-correlation coefficients (the first row of Fig. 8), the synthetic waveforms do not fit the EGFs well. At periods of 25–50 s, the cross-correlation coefficients are positively distributed, indicating that the phase lag time is less than one-fourth of the central period (consistent with Fig. 7a). On the other hand, the existence of negative correlation coefficients at shorter periods corresponds to lag times larger than one-fourth of the central period.

CUB

Compared with CRUST2.0, CUB predicts relatively better-fitting phase arrivals. There exists a moderately negative linear trend between phase delay time and interstation distance, except at periods of 25–50 s (the second row of Figs. 6 and 7). The χ^2/N values are large (~10–26) with

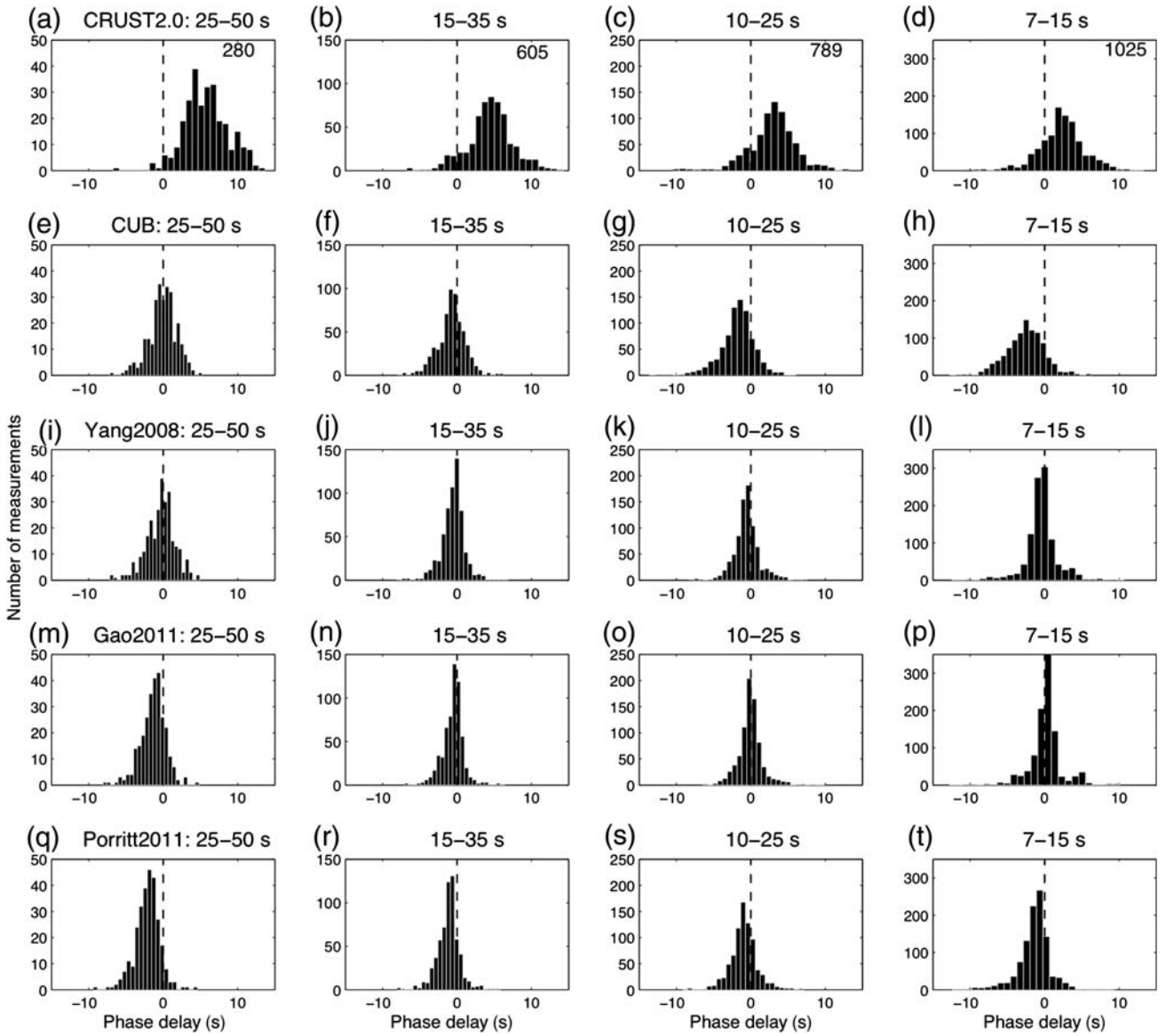

Figure 7. Histograms of cross-correlation lag times between the EGFs and synthetics for five models (each row) at four frequency bands (each column) with stations distributed over the whole study area. The data set is the same as in Figure 6. The dashed lines mark zero delay time. A positive delay time means that the phase arrival in the EGFs is later than in the synthetics, indicative of a velocity model that is too fast. The number of measurements used at each frequency band is denoted in panels (a)–(d).

an increasing standard deviation of phase delays toward short periods. On average, the synthetic arrivals are systematically delayed compared with the observations (the second row of Fig. 7), indicating a slower average crustal velocity than the true Earth crust. At periods of 25–50 s, phase delays appear less scattered with relatively smaller χ^2/N values (~7), which indicate that CUB has a better velocity resolution in the uppermost mantle than in the crust.

Models of Yang2008 and Gao2011

The results by Yang2008 and Gao2011 are similar (the third and fourth rows in Figs. 6–8, respectively), with χ^2/N values less than 10. One reason that these two models generate similar results is that Gao2011 was constructed using Yang2008 as a reference model (Gao *et al.*, 2011). There is no obvious dependence of phase delay time on interstation distance as displayed by CRUST2.0 and CUB. The generally good prediction of phase arrival times is supported by the unimodal distribution of cross-correlation coefficients with the mean greater than 0.5 (Fig. 8). The standard deviation of phase delays (relative to zero mean) is about 1.5 times smaller than for CUB, and the χ^2/N values are up to 4 times smaller, indicating a better-resolved average velocity structure. The χ^2/N value and standard deviation of phase delays reach their minimum values at periods of 15–35 s for both models (Fig. 6). However, both the standard deviation of phase delays and χ^2/N increase at the shortest period (7–15 s), and the cross-correlation coefficients gradually

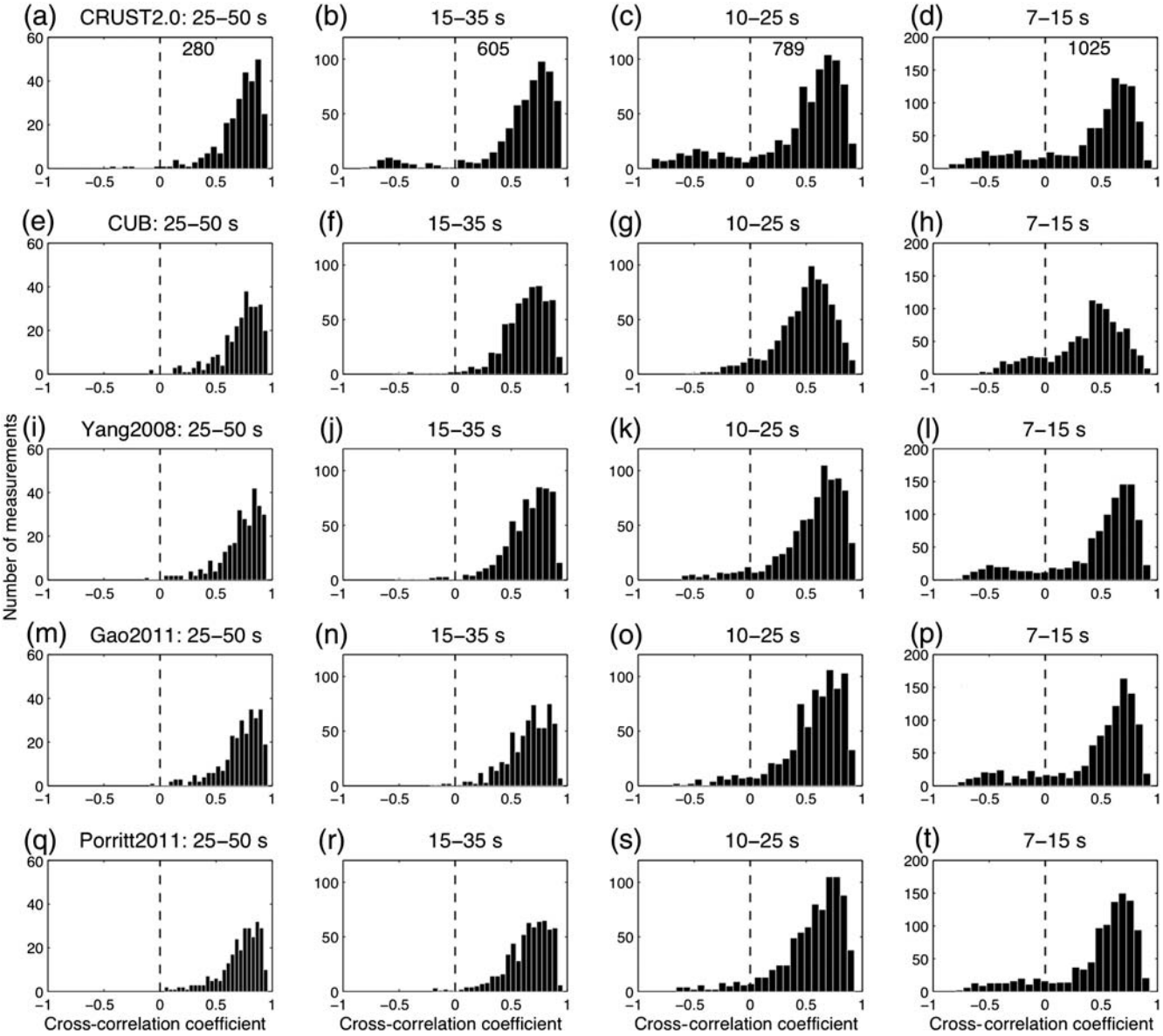

Figure 8. Histograms of cross-correlation coefficients between EGFs and synthetics for five models (each row) at four frequency bands (each column). Negative cross-correlation coefficients indicate that the phase lag time exceeds one-fourth of the central period. Annotations are the same as in Figure 7.

become more scattered when moving from longer to shorter periods (Fig. 8). This may indicate that the complexity of the crustal structure is not fully explained by the two models.

Model of Porritt2011

A weakly linear trend is observed between phase delay time and interstation distance for Porritt2011, indicating a slower average velocity than the true Earth, which is similar to the CUB model. It corresponds to large χ^2/N values (~8–15) and standard deviations of phase delays. Compared with other models, Porritt2011 has two low-velocity layers in the crust, including a very-low-velocity sedimentary layer near the surface and a low-velocity midcrust, as shown by the average 1D velocity profile (Fig. 1). Both low-velocity layers may delay the phase arrival in the synthetics, particularly at the shortest periods (Fig. 6), which are more sensitive to the upper- and midcrust structure. Similar to what is observed for the other models, a portion of the phase delay times at short periods (10–25 and 7–15 s) exceeds one-fourth of the central period, resulting in negative cross-correlation coefficients (the last row of Fig. 8).

Discussion and Conclusions

In this study, we test and validate five velocity models of the Pacific Northwest with a 3D finite-difference method. The cross correlation of the EGFs and synthetic waveforms allows for a systematic comparison of the models. In general, the synthetic Green's functions from the shear-wave velocity

models of Yang2008, Gao2011, and Porritt2011 match the observed EGFs better than in the cases of CRUST 2.0 and CUB (Figs. 6–8). This indicates an improvement of the crust and uppermost mantle structure that is resolved by surface-wave tomography in the Pacific Northwest. The fact that the phase delay time for CRUST 2.0 is linearly dependent on interstation distance and is dominantly positive suggests that this model is, on average, too fast for the Pacific Northwest. Similarly, the weakly negative linear trend of delay time with distance by CUB and Porritt2011 indicates a lower-than-actual average velocity for the study area. In contrast, there is no linear trend between the phase delay time and interstation distance for the models of Yang2008 and Gao2011 (Fig. 6). The phase arrival of the EGFs is well predicted with relatively smaller standard deviation (relative to zero mean) ànd χ^2/N values. At 25–50 s, with the corresponding sensitivity-kernel depth from the lower crust to uppermost mantle, the synthetics of Gao2011 and Porritt2011 are delayed on average (first column of Fig. 7). One possibility for the phase misfit could be the selection of the Moho depth. If the Moho interface in the models is deeper than its real depth, the average velocity around that depth would be slower, and the models would predict delayed synthetic phase arrivals compared with those observed. As discussed by Gao *et al.* (2011), the average Moho depth in their study is ~4 km deeper than that of Yang *et al.* (2008). The average Moho depth in Porritt *et al.* (2011) appears to be even deeper than the other two models (by comparing Fig. 3 in Porritt *et al.* [2011] and Fig. S2 in Gao *et al.* [2011]).

There are a few approximations in the velocity models and wave simulation that may also contribute to the misfit between the empirical and synthetic Green's functions. First, all of the models tested in this study are isotropic, and no anisotropy is considered in wave simulation. However, strong anisotropy exists in the crust and upper mantle of the western United States (e.g., Long *et al.*, 2009; Russo, 2009; Buehler and Shearer, 2010; Yuan and Romanowicz, 2010) and may account for a significant part of the shear-wave velocity variations (Moschetti *et al.*, 2010). Second, the conversion of shear-wave velocity to *P*-wave velocity in wave simulation assumes a constant Poisson's ratio in the crust and applies the empirical relationship of V_P, V_S, and density in the mantle. As shown by Eagar *et al.* (2011), the Poisson's ratio varies within the ~0.20–0.35 range in the crust, corresponding to a V_P/V_S ratio of ~1.6–2.1. This may result in up to ±10% *P*-wave velocity variation in the V_S-to-V_P conversion, though only the V_P in the shallowest crust affects Rayleigh waves (< 10 km for up to 50-s period Rayleigh waves). For scale, a ±10% *P*-wave velocity variation in the upper ~15-km crust can result in up to ±1.5 s phase arrival time change for a Rayleigh wave with a period of 25–50 s and traveling between two stations separated by ~580 km. Third, both velocity models and wave simulation do not account for attenuation. This may result in inaccurate synthetic waveforms (e.g., Dalton *et al.*, 2009; Lawrence and Prieto, 2011), though the effect on phase delay is likely minor.

The existing crust and uppermost mantle velocity models in the Pacific Northwest need to be improved, as none of the normalized χ^2/N values are close to 1. The Pacific Northwest has the capability of generating ~M 9 megathrust earthquakes (Satake *et al.*, 1996; Tsuji *et al.*, 1998); thus, it is critical to precisely estimate the ground motion for seismic hazard evaluation. This requires a high-resolution crustal velocity model. Furthermore, a well-resolved crust and upper-mantle velocity model is the essential structural framework to locate earthquakes, determine source mechanisms, and understand the tectonic processes.

Data and Resources

All of the continuous seismic data were obtained from the Incorporated Research Institutions for Seismology (IRIS) Data Management Center at www.iris.edu (last accessed April 2012).

Acknowledgments

We thank Yingjie Yang and Robert Porritt for providing their shear-wave velocity models of the western United States for the model testing and validation. We thank Robert Porritt and Richard Allen for their comments on the model comparison. Suggestions from several members of the University of Rhode Island (URI) seismology lab helped to improve the manuscript. We also thank the Associate Editor and two reviewers for their comments. This project is funded by the National Science Foundation Award EAR-0738779 and the U.S. Air Force Research Laboratory under Award FA9453-10-C-0217.

References

Barmin, M. P., M. H. Ritzwoller, and A. L. Levshin (2001). A fast and reliable method for surface wave tomography, *Pure Appl. Geophys.* **158,** no. 8, 1351–1375.

Bassin, C., G. Laske, and G. Masters (2000). The current limits of resolution for surface wave tomography in North America, *Eos Trans. AGU* **81,** abstract no. F897.

Bensen, G. D., M. H. Ritzwoller, M. P. Barmin, A. L. Levshin, F. Lin, M. P. Moschetti, N. M. Shapiro, and Y. Yang (2007). Processing seismic ambient noise data to obtain reliable broad-band surface wave dispersion measurements, *Geophys. J. Int.* **169,** 1239–1260, doi: 10.1111/j.1365-246x.2007.03374.x.

Bozdag, E., and J. Trampert (2010). Assessment of tomographic mantle models using spectral element seismograms, *Geophys. J. Int.* **180,** 1187–1199.

Brocher, T. M. (2005). Empirical relations between elastic wavespeeds and density in the Earth's crust, *Bull. Seismol. Soc. Am.* **95,** no. 6, 2081–2092.

Buehler, J. S., and P. M. Shearer (2010). *Pn* tomography of the western United States using USArray, *J. Geophys. Res.* **115,** no. B09315, doi: 10.1029/2009JB006874.

Burdick, S., C. Li, V. Martynov, T. Cox, J. Eakins, T. Mulder, L. Astiz, F. L. Vernon, G. L. Pavlis, and R. D. van der Hilst (2008). Upper mantle heterogeneity beneath North America from travel time tomography with global and USArray transportable array data, *Seismol. Res. Lett.* **79,** 384–392.

Calkins, J. A., G. A. Abers, G. Ekström, K. C. Creager, and S. Rondenay (2011). Shallow structure of the Cascadia subduction zone beneath western Washington from spectral ambient noise correlation, *J. Geophys. Res.* **116,** no. B07302, doi: 10.1029/2010JB007657.

Calvert, A. J., L. A. Preston, and A. M. Farahbod (2011). Sedimentary underplating at the Cascadia mantle-wedge corner revealed by seismic imaging, *Nat. Geosci.* **4,** doi: 10.1038/NGEO1195.

Christensen, N. I., and W. D. Mooney (1995). Seismic velocity structure and composition of the continental crust: A global view, *J. Geophys. Res.* **100,** 9761–9788.

Dalton, C. A., G. Ekström, and A. M. Dziewonski (2009). Global seismological shear velocity and attenuation: A comparison with experimental observations, *Earth Planet. Sci. Lett.* **284,** 65–75.

Eagar, K. C., M. J. Fouch, D. E. James, and R. W. Carlson (2011). Crustal structure beneath the High Lava Plains of eastern Oregon and surrounding regions from receiver function analysis, *J. Geophys. Res.* **116,** no. B02313, doi: 10.1029/2010JB007795.

Ekström, G., G. A. Abers, and S. C. Webb (2009). Determination of surface-wave phase velocities across USArray from noise and Aki's spectral formulation, *Geophys. Res. Lett.* **36,** L18301, doi: 10.1029/2009GL039131.

Gao, H., E. D. Humphreys, H. Yao, and R. D. van der Hilst (2011). Crust and lithosphere structure of the northwestern U.S. with ambient noise tomography: Terrane accretion and Cascade arc development, *Earth Planet. Sci. Lett.* **304,** doi: 10.1016/j.epsl.2011.01.033.

Kennett, B. L. N., E. R. Engdahl, and R. Buland (1995). Constraints on seismic velocities in the Earth from travel times, *Geophys. J. Int.* **122,** 108–124.

Lawrence, J. F., and G. A. Prieto (2011). Attenuation tomography of the western United States from ambient seismic noise, *J. Geophys. Res.* **116,** no. B06302, doi: 10.1029/2010JB007836.

Lebedev, S., and R. D. van der Hilst (2008). Global upper-mantle tomography with the automated multimode inversion of surface and *S*-wave forms, *Geophys. J. Int.* **173,** doi: 10.1111/j.1365-246X.2008.03721.x.

Long, M. D., H. Gao, A. Klaus, L. S. Wagner, M. J. Fouch, D. E. James, and E. D. Humphreys (2009). Shear wave splitting and the pattern of mantle flow beneath eastern Oregon, *Earth Planet. Sci. Lett.* **288,** doi: 10.1016/j.epsl.2009.09.039.

Ma, S., G. A. Prieto, and G. C. Beroza (2008). Testing community velocity models for southern California using the ambient seismic field, *Bull. Seismol. Soc. Am.* **98,** no. 6, 2694–2714, doi: 10.1785/0120080947.

Maceira, M., C. A. Rowe, R. M. Allen, and M. J. Obrebski (2010). Validating 3D seismic velocity models using the spectral element method, *AGU* Fall meeting, abstract no. S43B-2079.

Montagner, J.-P. (1986). Regional three-dimensional structures using long-period surface waves, *Ann. Geophys.* **4,** 283–294.

Montelli, R., G. Nolet, G. Masters, F. A. Dahlen, and S.-H. Hung (2004). Global *P* and *PP* traveltime tomography: Rays versus waves, *Geophys. J. Int.* **158,** 637–654, doi: 10.1111/j.1365-246X.2004.02346.x.

Moschetti, M. P., M. H. Ritzwoller, F.-C. Lin, and Y. Yang (2010). Crustal shear wave velocity structure of the western United States inferred from ambient seismic noise and earthquake data, *J. Geophys. Res.* **115,** no. B10306, doi: 10.1029/2010JB007448.

Porritt, R. W., R. M. Allen, D. C. Boyarko, and M. R. Brudzinski (2011). Investigation of Cascadia segmentation with ambient noise tomography, *Earth Planet. Sci. Lett.* **309,** 67–76, doi: 10.1016/j.epsl.2011.06.026.

Roth, J. B., M. J. Fouch, D. E. James, and R. W. Carlson (2008). Three-dimensional seismic velocity structure of the northwestern United States, *Geophys. Res. Lett.* **35,** L15304, doi: 10.1029/2008GL034669.

Russo, R. M. (2009). Subducted oceanic asthenosphere and upper mantle flow beneath the Juan de Fuca slab, *Lithosphere* **1,** 195–205, doi: 10.1130/L41.1.

Sabra, K. G., P. Roux, and W. A. Kuperman (2005). Emergence rate of the time-domain Green's function from the ambient noise cross-correlation function, *J. Acoust. Soc. Am.* **118,** 3524–3531.

Satake, K., K. Shimazaki, Y. Tsuji, and K. Ueda (1996). Time and size of a giant earthquake in Cascadia inferred from Japanese tsunami records of January 1700, *Nature* **378,** 246–249.

Schmandt, B., and E. D. Humphreys (2010). Complex subduction and small-scale convection revealed by body-wave tomography of the western United States upper mantle, *Earth Planet. Sci. Lett.* **297,** 435–445, doi: 10.1016/j.epsl.2010.06.047.

Shapiro, N. M., and M. H. Ritzwoller (2002). Monte-Carlo inversion for a global shear velocity model of the crust and upper mantle, *Geophys. J. Int.* **151,** 88–105.

Shen, Y., Y. Ren, H. Gao, and B. Savage (2012). An improved method to extract very broadband empirical Green's functions from ambient seismic noise, *Bull. Seismol. Soc. Am.* **102,** no. 4, 1872–1877.

Simons, F. J., and R. D. van der Hilst (2003). Seismic and mechanical anisotropy and the past and present deformation of the Australian lithosphere, *Earth Planet. Sci. Lett.* **211,** 271–286, doi: 10.1016/S0012-821X(03)00198-5.

Snieder, R. (2004). Extracting the Green's function from the correlation of coda waves: A derivation based on stationary phase, *Phys. Rev. E.* **69,** 046610.

Stankiewicz, J., T. Ryberg, C. Haberland, Fauzi, and D. Natawidjaja (2010). Lake Toba volcano magma chamber imaged by ambient seismic noise tomography, *Geophys. Res. Lett.* **37,** L17306, doi: 10.1029/2010GL044211.

Stehly, L., M. Campillo, and N. M. Shapiro (2007). Traveltime measurements from noise correlation: Stability and detection of instrumental time-shifts, *Geophys. J. Int.* **171,** 223–230, doi: 10.1111/j.1365-246X.2007.03492.x.

Tsuji, Y., K. Ueda, and K. Satake (1998). Japanese tsunami records from the January 1700 earthquake in the Cascadia subduction zone, *Zisin* **51,** 1–17 (in Japanese with English abstract).

Villaseæor, A., Y. Yang, M. H. Ritzwoller, and J. Gallart (2007). Ambient noise surface wave tomography of the Iberian Peninsula: Implications for shallow seismic structure, *Geophys. Res. Lett.* **34,** L11304, doi: 10.1029/2007GL030164.

Wagner, L., D. W. Forsyth, M. J. Fouch, and D. E. James (2010). Detailed three-dimensional shear wave velocity structure of the northwestern United States from Rayleigh wave tomography, *Earth Planet. Sci. Lett.* **299,** 273–284, doi: 10.1016/j.epsl.2010.09.005.

Yang, Y., M. H. Ritzwoller, F.-C. Lin, M. P. Moschetti, and N. M. Shapiro (2008). Structure of the crust and uppermost mantle beneath the western United States revealed by ambient noise and earthquake tomography, *J. Geophys. Res.* **113,** no. B12310, doi: 10.1029/2008JB005833.

Yao, H., C. Beghein, and R. D. van der Hilst (2008). Surface wave array tomography in SE Tibet from ambient seismic noise and two-station analysis—II. Crustal and upper-mantle structure, *Geophys. J. Int.* **173,** 205–219, doi: 10.1111/j.1365-246X.2007.03696.x.

Yao, H., R. D. van der Hilst, and M. V. de Hoop (2006). Surface-wave array tomography in SE Tibet from ambient seismic noise and two-station analysis—I. Phase velocity maps, *Geophys. J. Int.* **166,** no. 2, 732–744, doi: 10.1111/j.1365-246X.2006.03028.x.

Yuan, H., and B. Romanowicz (2010). Depth dependent azimuthal anisotropy in the western US upper mantle, *Earth Planet. Sci. Lett.* **300,** 385–394.

Zhang, W., Y. Shen, and L. Zhao (2011). Three-dimensional anisotropic seismic wave modeling in spherical coordinates by a collocated-grid finite difference method, *Geophys. J. Int.* **188,** 1359–1381, doi: 10.1111/j.1365-246X.2011.05331.x.

Zhang, Z., and Y. Shen (2008). Cross-dependence of finite-frequency compressional waveforms to shear seismic wave speeds, *Geophys. J. Int.* **174,** 941–948, doi: 10.1111/j.1365-246X.2008.03840.x.

Graduate School of Oceanography
University of Rhode Island
Room 205, Horn Lab
215 South Ferry Road
Narragansett, Rhode Island 02882

Manuscript received 1 December 2011